Towards digitally programmed nonlinear electroacoustic resonators for low amplitude sound pressure levels: Modeling and experiments

Maxime Morell, Emmanuel Gourdon, Manuel Collet, Alireza Ture Savadkoohi, Emanuele de Bono, Claude-Henri Lamarque

Towards digitally programmed nonlinear electroacoustic resonators for low amplitude sound pressure levels: modeling and experiments

Maxime Morell[a], Emmanuel Gourdon[a], Manuel Collet[b], Alireza Ture Savadkoohi[a], Emanuele De Bono[b], Claude-Henri Lamarque[a]

[a] *Univ Lyon, ENTPE, Ecole Centrale de Lyon, CNRS, LTDS, UMR5513, 3 rue Maurice Audin, Vaulx-en-Velin, 69518, , France*
[b] *Univ Lyon, CNRS, Ecole Centrale de Lyon, ENTPE, LTDS, UMR5513, 36 av. Guy de Collongue, Ecully, 69130, , France*

Abstract

Passive acoustic foams have limitations in efficiently reducing low-frequency noise below 800 Hz due to the associated wavelengths for reasonable material thickness. To address this challenge, passive or semi-active resonators are commonly employed solutions. Linear resonators are very efficient within a narrow frequency bandwidth. However, nonlinear oscillators can broaden this bandwidth, but activation of their nonlinear responses typically requires high excitation amplitudes, beyond human hearing tolerance amplitudes. Furthermore, the specific type of nonlinearity in such devices is often predetermined by the inherent properties of the resonator. In this study, we employ a novel digital control algorithm, allowing to activate the nonlinear response of the electroacoustic resonator at low excitation amplitudes. This algorithm, which relies on real-time integration, facilitates the creation of nonlinear resonators featuring polynomial or diverse non-polynomial nonlinearities within the range of low amplitudes. The nonlinear control is carried out on a loudspeaker equipped with a microphone. Our research highlights the potential to create nonlinear resonators with different, versatile and programmable behaviors. Unprecedented non-polynomial nonlinear behaviors are experimentally exhibited, we consider cubic, piece-wise linear, and logarithmic nonlinearities. These behaviors are implemented and compared to a semi-analytic model to control an acoustic mode of a tube under conditions of low excitation amplitudes and frequencies.

Keywords: Programmable, Low amplitude, Electroacoustic Resonator, Noise Control, Cubic nonlinearity, piece-wise nonlinearity, logarithmic potential nonlinearity, non-polynomial nonlinearities

1. Introduction

Addressing noise and vibrations has remained a central objective of research efforts for a significant period of time [1]. To solve this particular matter, passive, active, and hybrid categories have been considered for mitigating vibrations and noises across many fields such as mechanics, aeronautics, and acoustics. In acoustics, passive noise control stands as the most widely employed approach. Indeed, acoustic foams are commonly used in the building industry. However, their absorption capabilities are limited to the frequencies above 1 kHz [2]. The efficiency of acoustic foams diminishes at lower frequencies due to their damping mechanism [3, 4]. To overcome these limitations, passive resonators are widely used such as Helmholtz resonators. These resonators are very efficient on a narrow frequency bandwidth focused around their resonating frequency. With the intention of finding solutions to these limitations, active noise cancellation technology emerged in 1878 with Rayleigh's experiment involving the superposition of sound fields using two synchronized tuning forks [5]. Lueg [6] wrote the first patent on noise cancellation using a wave in phase opposition with an incident wave. Then, active noise cancellation has been rapidly developed, supported by a substantial volume of articles published on the subject matter [7, 8, 9, 10]. However, active noise cancellation demands a substantial amount of energy to be efficient in spatial zones. Another active noise control method has been created and lies on Impedance Control (IC), with the original idea from Olson and May [11]. The IC consists of adapting the boundary conditions of a material or a device - usually a loudspeaker - to choose the absorption and reflection conditions to be applied on the incident wave by the material. Unlike active noise cancellation, this approach doesn't introduce additional waves, rendering the system acoustically passive. Building upon Olson and May's work [11], Guicking [12, 13] extended the IC concept to electroacoustic absorbers composed of a loudspeaker collocated to a microphone at normal incidence in a Kundt's tube. Furtoss and Thenail [14, 15] designed an IC system that created a quarter wavelength resonator using an accelerometer and a microphone to target specific impedances. Subsequently, the studies

focused on the active complex impedance control (e.g. see [16]) where the optimal impedance is targeted. The following works oriented to create a distributed network of electroacoustic absorber cells with a loudspeaker control based on the advection equation [17, 18, 19]. Following this, a model inversion control of the electroacoustic absorber has been created by targeting the optimal acoustic impedances at both normal and grazing incidences, with and without flow [20, 21, 22, 23]. Recently, a new kind of electroacoustic absorber has been designed using the concept of plasmacoustic metalayers to achieve broadband sound control [24].

Nonlinear phenomena in acoustics are not employed a lot for noise control, unlike mechanics where such behaviors are extensively explored and used for their benefits [25]. Indeed, nonlinear absorbers present faster decreases for transient regimes [26], or can feature targeted energy transfer phenomenon which consists of an irreversible energy transfer from a primary system to a nonlinear absorber. Furthermore, nonlinear systems can be designed to be efficient on large frequency bandwidths [26]. Extensive researches have been conducted on nonlinear behaviors, including the duffing type oscillators [27, 28], piece-wise oscillators [29, 30, 31, 32, 33, 34], or vibroimpact oscillators [35, 36], all aimed at mitigating vibrations. These studies have sparked interest in applying nonlinear principles to acoustic absorbers [37]. However, the activation of nonlinear phenomena is usually constrained by an amplitude threshold rarely reached. Indeed, this threshold is situated at amplitudes that pose the risk of permanently damaging a human ear. Bellet [38] implemented a visco-elastic membrane with an amplitude of 148 dB that behaves as a pure cubic oscillator, and showed multiple nonlinear phenomena, with both stationary and transient regimes, along with efficient control of the coupled acoustic mode. Gourdon [39, 40] placed a Helmholtz resonator in its nonlinear regime, above 138 dB and showed interesting noise reduction in the coupled tube. Bitar [41] attempted to create a passive nonlinear electroacoustic absorber with an analogic circuit. Finally, Guo [42] created a nonlinear electroacoustic absorber at hearing amplitudes around 95 dB thanks to an additional microphone in the back cavity of the loudspeaker giving the displacement of the membrane at each time step. This additional measurement is needed, as frequency-domain approaches cannot perform the creation of nonlinear behaviors, and permits the calculation of a polynomial nonlinear current to be added to a linear current implemented through frequency-domain approaches. In this study, unprecedented non-polynomial nonlinear behaviors are exhibited through an innovative method to digitally

program nonlinear Electroacoustic Resonator (ER) at low excitation amplitudes, without additional microphones in the back cavity of the loudspeaker. It is a real-time based method briefly presented in Section 2 and detailed in [43]. Subsequently, the ER is weakly coupled to an acoustic mode of a tube which is modeled in Section 3. Finally, experimental results are presented for multiple original programmed nonlinear behaviors and compared to the model in Section 4. The good correlation between numerical and experimental results confirms the achievement of nonlinear dynamics involving cubic, piece-wise, and logarithmic restoring force functions, and demonstrates the potentialities of such nonlinear behaviors for noise reduction and the control of acoustic modes.

2. The Electroacoustic Resonator

2.1. The concept

The underlying concept is to create an acoustic resonator with a loudspeaker collocated to a microphone, and equipped with a feedback control that runs by a dedicated processor. The study aims at creating programmable nonlinear resonators at low excitation amplitudes. The classical approach which relies on the Z-transform and the infinite impulse response experimental implementation [44] is not suitable for nonlinear resonators implementation due to its frequency-based approach. As a result, an innovative and efficient real-time-based method has been created to address this challenge. Assuming that the loudspeaker is positioned on its first mode, the algorithm carries out a pressure-based current-driven control of the membrane displacement. Indeed, it retrieves the measured pressure coming from the microphone and estimates the corresponding electrical current to send into the loudspeaker coil. Once the electrical current is delivered, the loudspeaker behaves as the programmed nonlinear resonator. Further details on the algorithm can be found in the next section, and in [43, 45].

2.2. Programming of the Electroacoustic Resonator

The algorithm considers the pressure as an input and the electrical current as an output. It estimates the electrical current based on the measured pressure to achieve the desired behavior of the loudspeaker. Given the low operational frequencies and amplitudes, the membrane is regarded as both rigid and planar. The loudspeaker is placed on its first mode, modeled as a single-degree-of-freedom oscillator.

The dynamic model of the loudspeaker's first mode is a classical mass-spring-damper:

$$M_0\ddot{u}_m(t) + R_0\dot{u}_m(t) + K_0 u_m(t) = S_d p(t) - Bli(t) \tag{1}$$

where $\dot{\bullet}$ represents the time derivative of the variable. u_m denotes the displacement of the membrane of the loudspeaker. M_0, R_0, and K_0 are the modal parameters of the loudspeaker's first mode without any applied current. Bli is the Laplace force, while B is the intensity of the magnetic field, and l the coil's length. $S_d p$ stands for the force induced by the incident acoustic waves, while S_d represents the effective area of the loudspeaker membrane [46]. The desired behavior equation can be written as:

$$M_d\ddot{u}_m(t) + R_d\dot{u}_m(t) + F_{\mathrm{NL}}(t, u_m) = S_d p(t) \tag{2}$$

where M_d, R_d, and K_d denote the desired modal parameters of the loudspeaker's first mode, and F_{NL} stands for a chosen nonlinear restoring forcing function. However, also a linear part of the stiffness of the loudspeaker should be taken into account in F_{NL} for stability issues. It is due to the impossibility to reach a zero stiffness system. It should be mentioned that in this study we suppose that F_{NL} is a nonlinear restoring forcing function i.e. $F_{\mathrm{NL}}(t, u_m)$, but generally speaking it can be $F_{\mathrm{NL}}(t, u_m, \dot{u}_m, \ddot{u}_m)$. The algorithm is now explained using Eqs. (1) and (2).

The algorithm is structured around two main tasks. The first task consists of the determination of the desired displacement, speed, and acceleration of the loudspeaker's membrane. To achieve this result, at time step t_n, the algorithm uses the measured pressure to integrate Eq. (2) with a numerical scheme. This real-time resolution predicts the desired displacement u_m and speed $\dot{u}_m$ for the next time step t_{n+1} and keeps the values in memory. At time step t_{n+1}, the algorithm uses the prediction of the desired displacement and speed done at time step t_n along with the newly measured pressure at time step t_{n+1} to estimate the desired acceleration $\ddot{u}_m$ using Eq. (2). Then, the second task is devoted to the calculation of the electrical current to send into the loudspeaker. From Eq. (1), the controller to enforce the desired displacement is given by:

$$i(t) = \frac{S_d}{Bl}\left(p(t) - \left(\frac{M_0}{S_d}\ddot{u}_m + \frac{R_0}{S_d}\dot{u}_m + \frac{K_0}{S_d}u_m\right)\right) \tag{3}$$

At time step t_{n+1}, and employing Eq. (3), the electrical current is computed using the previously determined desired displacement, speed and accelera-

tion, and the measured pressure.

3. Considered System

3.1. Principle and experimental set-up

This section aims at modeling the experimental acoustic set-up in order to predict the system behavior. The experimental set-up has been designed such that it can be modeled as a two-degrees-of-freedom system [38]. The model of the experiment is presented in Fig. 1 and has been widely studied in previous works [38, 37, 39]. It is composed of a cylindrical reduced section tube linked to the Electroacoustic Resonator through a cylindrical coupling box. The system is excited through an external loudspeaker (LS) placed at the opposite end of the tube. The microphone placed in the reduced section tube is employed to verify the noise attenuation performance achieved by our nonlinear ER, and it does not play a role in the programming. In the following parts, each segment of the experimental set-up will be explained in detail and will be modelized.

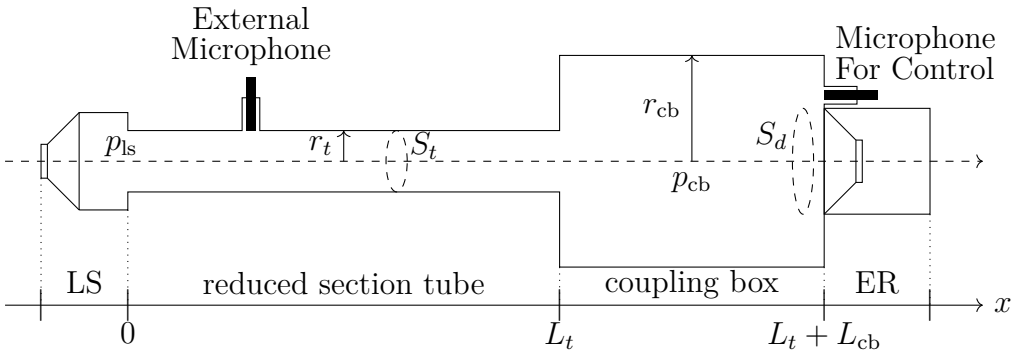

Figure 1: Scheme of the experimental set-up

3.2. Analytical modeling

This model assumes that waves are plane. The section of the largest tube of the experiment allows the first transverse modes to appear above 2 kHz. It ensures plane waves below this excitation frequency.

3.2.1. The acoustic source model

One of the innovations introduced in this work is the functionality of the proposed system at low excitation amplitude. As previously mentioned, acoustic resonators usually need to be excited at high excitation amplitudes to activate their nonlinear behaviors [40, 39, 38]. These sound pressure levels range from 120 dB to 160 dB depending on the characteristics of the device. The working frequency is chosen to bound the frequencies of the reduced section tube's first acoustic mode: from 350 Hz to 800 Hz. The acoustic source is modeled as an incident pressure at $x = 0$ (see Fig. 1), named p_{ls}.

3.2.2. The coupling box model

The goal of introducing the coupling box into the system is to maintain a weak coupling between the primary system to be controlled (the reduced section tube) and the added system (the ER). To achieve such a condition through the coupling box, its section is chosen to be large enough compared to the ones of the narrowed tube section and the membrane of the ER. Additionally, the length of the coupling box is kept relatively short compared to the wavelengths of the working frequencies to maintain a constant pressure within the box. Using the mass conservation equation, one can express the pressure in the coupling box, denoted p_{cb}, as a function of its volume variation:

$$p_{\mathrm{cb}}(t) = -\rho_0 c_0^2 \frac{\mathrm{d}V_{\mathrm{cb}}(t)}{V_{\mathrm{cb},0}} \tag{4}$$

where $V_{\mathrm{cb},0}$ represents the initial volume of the coupling box, ρ_0 is the air density, and c_0 is the velocity of the sound in the air. The variation of volume $\mathrm{d}V_{\mathrm{cb}}$ can be described in terms of displacements of the membrane of the ER and of the reduced section tube air mass. Equation (4) reads:

$$p_{\mathrm{cb}}(t) = k_b\Big(S_t u_a(t) - S_d u_m(t)\Big) \tag{5}$$

with $k_b = \frac{\rho_0 c_0^2}{V_{\mathrm{cb},0}}$.

3.2.3. The model of the reduced section tube

The reduced-section tube is considered with boundary conditions at each end of the tube that ensures the continuity of the displacements. These conditions are given in Eq. (11). From the mass conservation equation, one

can easily get the relation between the pressure p and the displacement of the air particles denoted as u_{air}:

$$p(x,t) = -\rho_0 c_0^2 \frac{\partial u_{\text{air}}}{\partial x}(x,t) \tag{6}$$

The Euler equation for a plane wave without flow reads:

$$\rho_0 \frac{\partial^2 u_{\text{air}}}{\partial t^2} = -\frac{\partial p}{\partial x} \tag{7}$$

By replacing Eq. (6) in Eq. (7), one can obtain:

$$\rho_0 \frac{\partial^2 u_{\text{air}}}{\partial t^2} = \rho_0 c_0^2 \frac{\partial^2 u_{\text{air}}}{\partial x^2} \tag{8}$$

Let $u^*_{\text{air}}(x,t)$ be a virtual displacement field that is kinematically admissible, continuous, and differentiable with respect to x and t. Multiplying Eq. (8) by $u^*_{\text{air}}(x,t)$ and integrating over the volume yields the variational formulation of Eq. (8):

$$\int_0^{L_t} \rho_0 \frac{\partial^2 u_{\text{air}}}{\partial t^2} S_t u^*_{\text{air}} \mathrm{d}x = \int_0^{L_t} \rho_0 c_0^2 \frac{\partial^2 u_{\text{air}}}{\partial x^2} S_t u^*_{\text{air}} \mathrm{d}x \tag{9}$$

After an integration by parts and using Eq (6) at $x = 0$, and $x = L_t$, this yields:

$$\begin{aligned} \int_0^{L_t} \rho_0 \frac{\partial^2 u_{\text{air}}}{\partial t^2} S_t u^*_{\text{air}} \mathrm{d}x = &- \int_0^{L_t} \rho_0 c_0^2 S_t \frac{\partial u_{\text{air}}}{\partial x} \frac{\partial u^*_{\text{air}}}{\partial x} \mathrm{d}x \\ &- S_t u^*_{\text{air}}(L_t,t) p_{\text{cb}} + S_t u^*_{\text{air}}(0,t) p_{\text{ls}} \end{aligned} \tag{10}$$

Let us suppose that the response of the system is dominated by its first mode, with the boundary conditions:

$$\begin{cases} u_{\text{air}}(0,t) = -u_{\text{ls}}(t) \\ u_{\text{air}}(L_t,t) = u_{\text{cb}}(t) \end{cases} \tag{11}$$

where the displacement is positive when the air goes out of the tube. We use a Rayleigh-Ritz method considering that:

$$u_{\text{air}}(x,t) = u_a(t)\Phi_1(x) = u_a(t)\Big(- \cos\Big(\frac{\pi x}{L_t}\Big)\Big) \tag{12}$$

where Φ_1 is the shape function (which represents also the first acoustic mode of the tube), and u_a stands for the modal coordinates. The same considerations are applied to the virtual displacement. Equation (10) yields to:

$$\Big(\frac{\rho_0 S_t L_t}{2}\Big)\ddot{u}_a + \Big(\frac{\rho_0 c_0^2 S_t \pi^2}{2L_t}\Big)u_a = -S_t(p_{\text{cb}} + p_{\text{ls}}) \tag{13}$$

We aim to have a model that closely represents the reality. However, the experiments revealed the need to model a damping coefficient. The choice of linear viscous damping is arbitrary. In typical structural or fluid-structure dynamics problems [47], it is often assigned a viscous term to synthesize the multi-physical phenomena contributing to the modal dissipation (such as mechanical damping and visco-thermal losses). The corresponding modal viscous coefficient is then usually estimated experimentally [48]. This formalism is kept in the reduced model by introducing a viscosity contribution in Eq (13), proportional to c_a. This parameter is obtained by experimental measurements and a brief study of its influence on the numerical results is presented in Appendix A.2. We obtain:

$$m_a\ddot{u}_a + c_a\dot{u}_a + k_a u_a = -S_t(p_{\text{cb}} + p_{\text{ls}}) \tag{14}$$

The modal mass m_a and modal stiffness k_a of the first acoustic mode of the reduced section tube reads:

$$\begin{cases} m_a = \dfrac{\rho_0 S_t L_t}{2} \\ k_a = \dfrac{\rho_0 c_0^2 S_t \pi^2}{2L_t} \end{cases} \tag{15}$$

3.2.4. Coupled equations of the two-degrees of freedom model

Each segment of the overall system has been described individually. Equations of the coupled systems can be constructed by incorporating boundary conditions. The considered ER model is given by the desired behavior equation Eq. (2) in the tube with the compatibility condition $p = p_{\text{cb}}$:

$$M_d\ddot{u}_m(t) + R_d\dot{u}_m(t) + F_{\text{NL}}(t, u_m) = S_d p_{\text{cb}}(t) \tag{16}$$

Equations (14) and (16) yield the system of equations:

$$\begin{cases} m_a\ddot{u}_a + c_a\dot{u}_a + k_a u_a = -S_t(p_{\text{cb}} + p_{\text{ls}}) \\ M_d\ddot{u}_m(t) + R_d\dot{u}_m(t) + F_{\text{NL}}(t, u_m) = S_d p_{\text{cb}}(t) \end{cases} \tag{17}$$

Introducing Eq. (5) into Eq. (17) yields the weakly coupled two-degree-of-freedom system of equations:

$$\begin{cases} m_a\ddot{u}_a + c_a\dot{u}_a + k_a u_a + S_t\big(k_b(S_t u_a - S_d u_m)\big) = -S_t p_{\text{ls}} \\ M_d\ddot{u}_m + R_d\dot{u}_m + F_{\text{NL}}(t, u_m) - S_d(k_b(S_t u_a - S_d u_m)) = 0 \end{cases} \tag{18}$$

We set $\gamma = k_b S_t S_d$ and $\alpha = S_d/S_t$. The system can be further rearranged as:

$$\begin{cases} m_a\ddot{u}_a + c_a\dot{u}_a + k_a u_a + \dfrac{\gamma}{\alpha}(u_a - \alpha u_m) = -S_t p_{\text{ls}} \\ M_d\ddot{u}_m + R_d\dot{u}_m + F_{\text{NL}}(t, u_m) + \gamma(\alpha u_m - u_a)) = 0 \end{cases} \tag{19}$$

It is worth noting that the weak coupling in this system appears to be non-reciprocal. Nevertheless, this is a consequence of formulating the equations in terms of forces. The formulation in terms of pressure, which is the common acoustic approach, results in a reciprocal coupling. In fact, the system of equations can be expressed using the acoustic parameters m_a/S_t, c_a/S_t, k_a/S_t, M_d/S_d and R_d/S_d:

$$\begin{cases} \dfrac{m_a}{S_t}\ddot{u}_a + \dfrac{c_a}{S_t}\dot{u}_a + \dfrac{k_a}{S_t}u_a + \dfrac{\gamma}{S_d}(u_a - \alpha u_m) = -p_{\text{ls}} \\ \dfrac{M_d}{S_d}\ddot{u}_m + \dfrac{R_d}{S_d}\dot{u}_m + \dfrac{1}{S_d}F_{\text{NL}}(t, u_m) + \dfrac{\gamma}{S_d}(\alpha u_m - u_a)) = 0 \end{cases} \tag{20}$$

The coupling between the mechanical behavior of the ER, and the acoustic behavior of the tube allows one to choose either of the formulations. In the following, the formulation in terms of forces defined Eq. (19) is employed.

4. Experimental results

4.1. Experimental set-up

The experimental set-up is described in Fig. 1 and shown in Fig. 2. The values of the parameters of the system are presented in Table 1. The ER is linked to a D-Space MicroLabBox DS1202 device which serves for programming and for the control of the loudspeaker displacement. The device operates with a sampling frequency of 50 kHz. The external excitation is produced by an external loudspeaker. The acoustic excitation lasts 60 seconds in the form of a linear chirp from 350 Hz to 800 Hz with either increasing or decreasing frequencies. Experiments are carried out with the coupled ER

r_t	1.45×10^{-2} m
S_t	6.61×10^{-4} m^2
L_t	0.204 m
r_{cb}	5.0×10^{-2} m
L_{cb}	0.125 m
S_d	1.3×10^{-3} m^2

Table 1: Values of parameters of the system

M_0	3.89×10^{-4} kg
R_0	2.63×10^{-1} kg.s^{-1}
K_0	4.34×10^{3} kg.s^{-2}
Bl/S_d	136.7 kg.m^{-1}.A^{-1}.s^{-2}

Table 2: Values of the modal parameters of the first mode of the loudspeaker when the current is set to zero.

and with a rigid termination. All results are confronted with those obtained from numerical integration of system equations. The modal parameters of the ER loudspeaker are detailed in Table 2. Desired parameters of the target dynamics are μ_M, μ_R, and μ_K, defined as follows:

$$\begin{cases} M_d = \mu_M M_0 \\ R_d = \mu_R R_0 \\ K_d = \mu_K K_0 \end{cases} \tag{21}$$

To illustrate the functionality of the programming at low excitation amplitudes, a variety of nonlinear behaviors are exploited and subjected to experimental testing.

To begin with, a cubic stiffness force is considered. It is a classic case that has been extensively studied across multiple domains [27, 26, 38]. Another nonlinear behavior considered is a piece-wise linear restoring forcing function, which has also been widely studied in fields such as mechanics [29, 31, 32, 33, 49]. However, its implementation in acoustics remains unprecedented and is implemented here. Finally, a logarithmic potential function is also studied, which leads to a non-polynomial restoring function. This force has shown the capability to induce targeted energy transfer as demonstrated by Gendelman in [50], and is experimentally implemented here for the first time. Each nonlinear behavior is compared to an optimized linear

resonator, whose behavior resembles a Tuned Mass Damper in mechanics. However, it is worth noting that the linear oscillator is optimized, while the nonlinear resonator is not. Optimization of such nonlinear behavior for noise reduction would need an additional and complete study, and will be addressed in future research. Notice that the presented behaviors can be replicated at lower or higher excitation amplitudes in the limits of the sensors and actuator capabilities. It is possible thanks to the ability to adjust β_{NL} which controls the threshold for nonlinear behavior activation [43]. A demonstration is carried out showcasing a measure at higher excitation amplitudes with the logarithmic potential restoring force in Fig. 13.

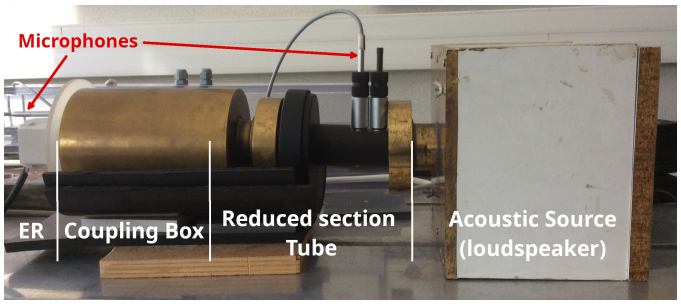

Figure 2: Experimental set-up

4.2. The cubic restoring forcing function

4.2.1. Design

As a first example, a cubic restoring forcing function is employed here to demonstrate the functionality of the nonlinear programming. The specific form of the nonlinear restoring force is given by:

$$F_{\mathrm{NL}}(t, u_m) = K_d(u_m + \beta_{\mathrm{NL}} u_m^3) \tag{22}$$

Where β_{NL} represents an adjustable nonlinear parameter. The value of the parameter β_{NL} plays a crucial role in determining whether the stiffness force composed of the linear part $K_d u_m$ and of the nonlinear part $K_d \beta_{\mathrm{NL}} u_m^3$ exhibits nonlinear phenomena across the considered range of amplitudes. The order of magnitude of these two parts weighs in the activation of nonlinear behavior. The sign of β_{NL} gives the sign of the force that determines whether the programmed behavior results in either a hardening or softening behavior. For considered amplitudes, the parameter is set to $\beta_{\mathrm{NL}} = 2 \times 10^{11}$ m^{-2} for

designing hardening behavior, and $\beta_{\mathrm{NL}} = -3 \times 10^{11}$ m^{-2} for designing softening behavior. The restoring forces for both cases are plotted in Fig. 3. In the case of the softening behavior, the overall potential can become positive at high oscillating amplitudes, leading to possible instability due to the injection of energy into the system. This case is used for illustrative purposes. Nevertheless, the logarithmic restoring force, later considered in this paper, solves the instability issue.

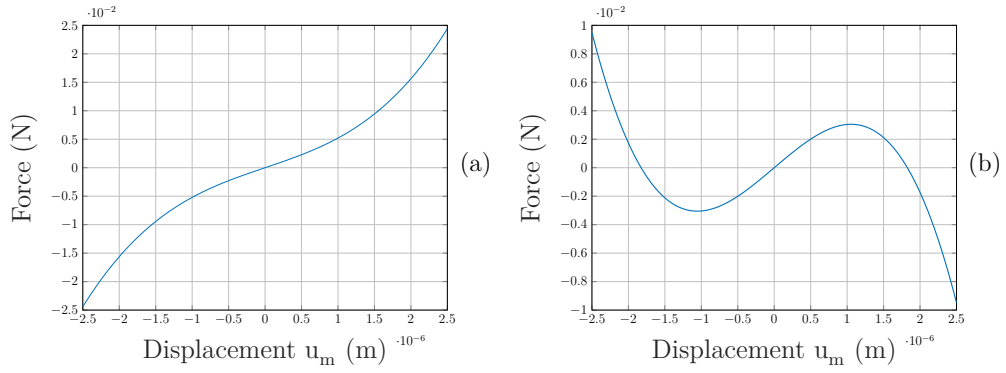

Figure 3: Nonlinear restoring force $F_{\mathrm{NL}} = K_d u_m + K_d \beta_{\mathrm{NL}} u_m^3$ for (a) hardening behavior $\beta_{\mathrm{NL}} = 2 \times 10^{11}$ m^{-2} and for (b) softening behavior $\beta_{\mathrm{NL}} = -3 \times 10^{11}$ m^{-2}.

The choice of the damping parameter μ_R is motivated by the need to create bifurcations. Indeed, a condition on the existence of the bifurcations emerges from the calculations of the centre manifold [51]. The given condition is expressed as a function of the linear stiffness and of the damping of the resonator. Throughout the paper, the choice of $\mu_R = 1/8$ ensures the existence of the bifurcation.

The choice of the linear stiffness parameter μ_K is motivated by the necessity to align the nonlinear resonance frequencies of the ER with the frequencies of the acoustic mode of the tube. Indeed, the nonlinear softening behavior involves large amplitude oscillations of the ER at lower frequencies, and as a result, the ER is more efficient within the considered frequency bandwidth. The choice of μ_K determines the frequency of the linear resonance of the ER. It allows the selection of the targeted linear mode frequency of the resonator. Choosing an appropriate μ_K is essential to tune the ER nonlinear resonance with the acoustic tube resonance for improved sound

absorption. Let f_t be the targeted frequency of the linear resonance of the ER, and f_0 be the frequency of the intrinsic mode of the ER. For simplicity, in this paper, μ_M is set to 1. The parameter μ_K can be found using the following equation:

$$\frac{\mu_K}{\mu_M} = \left(\frac{f_t}{f_0}\right)^2 \tag{23}$$

The choice of this parameter depends on the intensity of the considered nonlinearity. The parameter μ_K has been chosen by empirical and numerical means. The chosen parameters for the creation of hardening behavior are $\mu_M = \mu_K = 1$, and $\mu_R = 1/8$.

Knowing that $f_0 = 531$ Hz, the frequency gap between the linear first mode of the ER and the acoustic mode of the tube (596 Hz) is 65 Hz. In order to produce the nonlinear softening behavior, the parameter μ_K is chosen such as the frequency gap between the mode of the ER and the acoustic mode of the tube should be close to 65 Hz. Consequently, $f_t = 660$ Hz, which gives the parameters $\mu_M = 1$, $\mu_K = 1.5496$, and $\mu_R = 1/8$ for producing the softening behavior.

4.2.2. Results

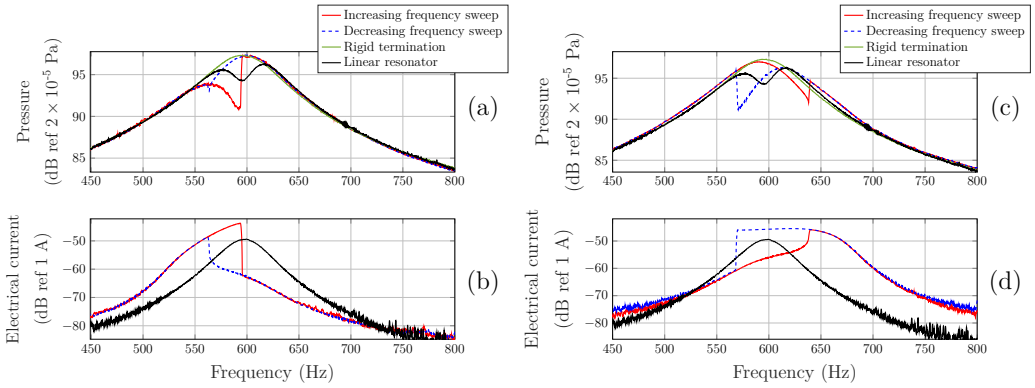

Figure 4: Experimental results for the cubic restoring force: variation of the pressure amplitude for the system with (a) hardening behavior, (c) softening behavior. Variation of the electrical current amplitude for the system with (b) hardening behavior, (d) softening behavior.

The variation of the pressure and electrical current amplitudes are plotted in Fig. 4 for both increasing and decreasing frequency sweep, and for the programmed hardening and softening behaviors. Variations of the electrical

current depicted in Fig. 4b clearly indicate the programming of a hardening behavior. Indeed, in the case of increasing frequency excitation, the measured pressure jumps (at 596 Hz) to a lower energy stable equilibrium point, whereas, in the case of decreasing frequency excitation, the measured pressure jumps (at 563 Hz) to a higher energy equilibrium point. For the softening behavior, shown in Fig. 4d, the opposite phenomenon occurs. The decreasing frequency measurement experiences a jump to lower energy equilibrium points at lower frequencies (569 Hz), while the increasing frequency measurement jumps to a higher energy equilibrium point (638 Hz). The pressure plotted in Fig. 4a and 4c presents the coupled behavior of the acoustic mode of the tube. The same phenomena occurs in both cases characterized by a significant reduction of the sound level in the tube at the frequencies corresponding to the nonlinear resonance. It is due to the activation of the ER nonlinear behavior that starts to act with large response amplitudes, and as a result it pumps the energy of the tube mode. However, from Fig. 4c one can observe a slight increase in the sound level in the reduced section tube from 600 Hz to 700 Hz. This issue can be solved by optimization means, which is out of the scope of the present study.

The results obtained from the numerical integration of the model outlined in

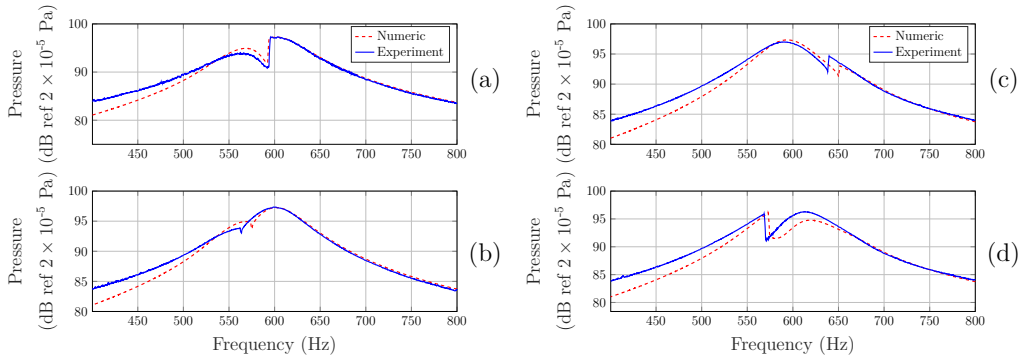

Figure 5: Experimental and corresponding numerical results obtained from direct numerical integration of Eq. (19): variation of the pressure amplitude for the hardening behavior with (a) increasing frequency sweep, (b) decreasing frequency sweep and for the softening behavior with (c) increasing frequency sweep, (d) decreasing frequency sweep.

Section 3 are compared to the experimental ones, and the outcomes are presented in Fig. 5. One can see that the model describes correctly the behavior of the coupled experimental system despite a noticeable frequency shift of the bifurcations illustrated in Fig 5. This shift can mainly be explained by model

uncertainties. Among model uncertainties, an important role is played by the S_d parameter, which can differ significantly from the membrane surface area. In terms of modeling, it is worth highlighting that the parameter S_d imposes significant challenges when it comes to its estimation and measurement [46]. This parameter affects the coupling between the acoustic mode and the ER, and hence the bifurcation frequencies. The inaccurate approximation at low frequencies is due to the presence of a coupling of an anti-resonance at lower frequencies that is not modeled. It might also be responsible for the frequency shift of the bifurcations. The influence of the antiresonance is discussed in Appendix A.1. Nevertheless, despite the strong approximations employed

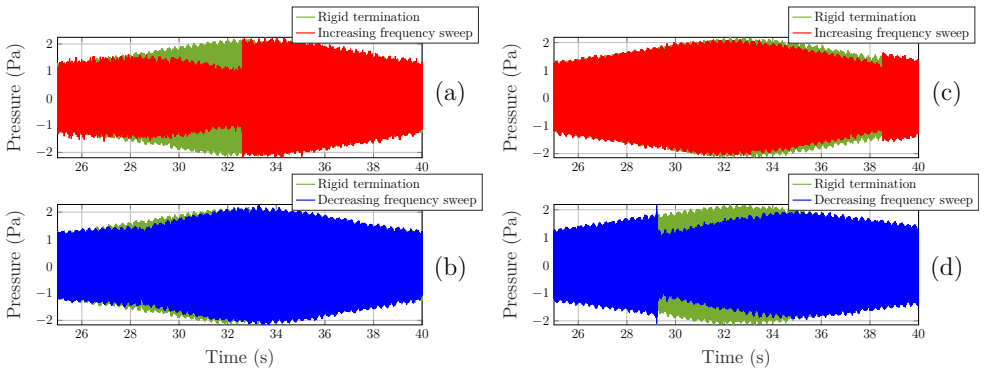

Figure 6: Experimental time histories for the cubic restoring force: pressure inside the reduced-section tube for the hardening behavior with (a) increasing frequency sweep (b) decreasing frequency sweep and for the softening behavior with (c) increasing frequency sweep (d) decreasing frequency sweep.

in the reduced numerical model, it well captures the trends of the measured pressure. It confirms that the actual behavior of the ER is extremely close to the desired behavior. As a result, the sound level starting point of the model is different from the experiment, modifying the amplitudes and so the frequencies of the bifurcations. Moreover, either larger frequency bandwidth or better sound absorption are realized using these cubic restoring forces. The tuning parameters should be optimized in future studies. Experimental time histories of the pressure inside the reduced-section tube are plotted in Fig. 6 for both hardening and softening behaviors. One can see that the incident pressure level is divided by two for the increasing frequency sweep, which is coherent with the reduction of more than 3 dB seen in the frequency plots. The bifurcation and its frequency are clearly recognizable.

4.3. The piece-wise linear restoring forcing function

4.3.1. Design

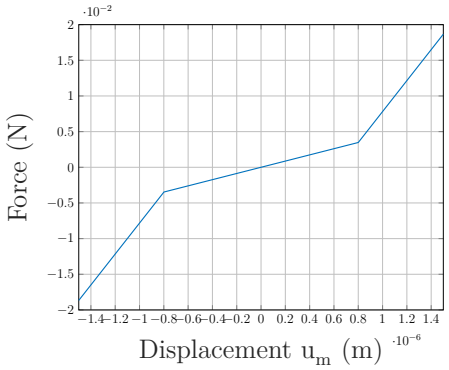

Figure 7: Piece-wise linear restoring forcing function.

The linear piece-wise potential behavior, which has not been previously explored in the context of acoustics, is introduced in this study. This behavior shows that the method presented here is not limited to smooth restoring forcing functions and can be applied to synthesize non-smooth functions as well. Here, the goal is to create a system with a hardening behavior similar to a duffing-type behavior with 2 different slopes depending on a clearance of 2δ. The associated restoring forcing function force plotted in Fig. 7 reads:

$$F_{\mathrm{NL}}(t, u_m) = \begin{cases} K_2 u_m - (K_1 - K_2)\delta & \text{if } u_m < -\delta \\ K_1 u_m & \text{if } -\delta < u_m < \delta \\ K_2 u_m + (K_1 - K_2)\delta & \text{if } \delta < u_m \end{cases} \tag{24}$$

This force is not differentiable on its whole definition domain, as in $u_m = \pm\delta$, where an infinite number of derivatives exist. The force is plotted in Fig. 7 for the values presented in Table 3. The clearance parameter 2δ defines the displacement of the membrane threshold at which nonlinear phenomena are initiated.

The selected parameters for the experiment are $\mu_M = 1$, $\mu_K = 1.2598$, and $\mu_R = 1/8$. The selection of μ_K has been driven by the aim of aligning the linear resonance frequency of the ER with the acoustic mode of the tube.

δ	8×10^{-7} m
K_1	K_d
K_2	$5K_1$

Table 3: Values of the piece-wise linear experiment. (see Eq. (21))

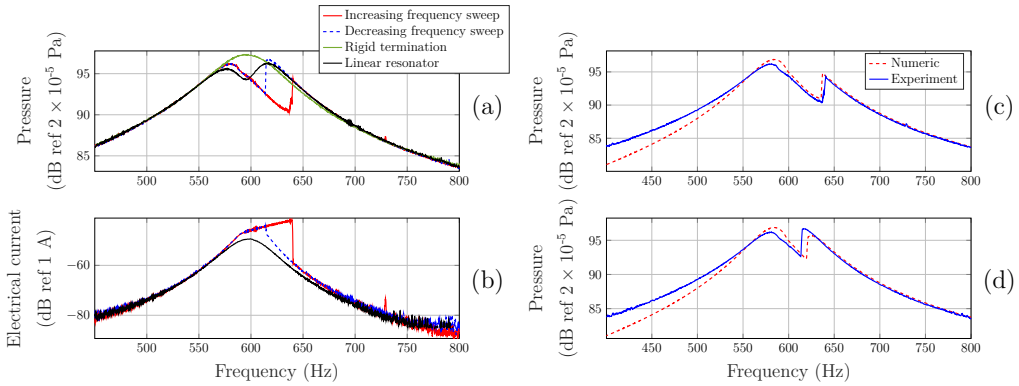

Figure 8: Experimental results for the piece-wise linear restoring force: variation of (a) the pressure amplitude (b) the electrical current. Experimental and corresponding numerical results obtained from direct numerical integration of Eq. (19): variation of the pressure amplitude with (a) Increasing frequency sweep, (b) Decreasing frequency sweep.

4.3.2. Results

The variations of the pressure and electrical current amplitudes are plotted in Fig. 8a and Fig. 8b. One can observe in Fig. 8b that the created behavior looks like a hardening duffing-type oscillator which is depicted in Fig. 4b. Moreover, a significant reduction of the sound level can be seen and is not limited to the frequencies of the nonlinear resonance. It is explained by the linear nature of the oscillator which is tuned to the frequency of the first mode of the primary system. The linear oscillator pumps the energy before activating its nonlinear behavior. This leads to a shift of the nonlinear behavior to higher frequencies, and as a result to energy pumping shifted from the maximum peak amplitude of the primary system. The experimental outcome is compared to results obtained from numerical integration of Eq. (19) for increasing frequency sweep in Fig. 8c and decreasing frequency sweep in Fig. 8d. Both results fit closely the measurements, confirming that the actual behavior follows the programmed piece-wise linear behavior. These results show that via accurate choice of parameters, the programming of the piece-wise linear restoring forcing function can lead to promising re-

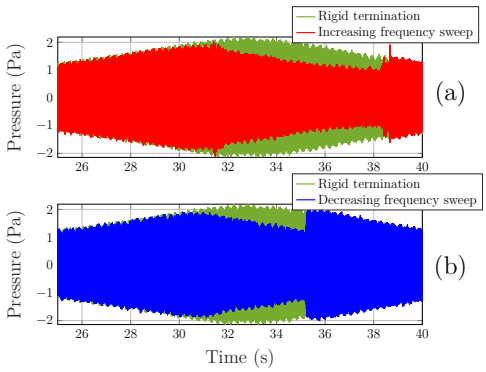

Figure 9: Experimental time histories for the piecewise linear restoring force: pressure inside the reduced-section tube for the hardening behavior with (a) increasing frequency sweep (b) decreasing frequency sweep.

sults. Indeed, this behavior shows the potential of such nonlinear ER, as the performed sound absorption is greater than the linear ER for a larger frequency bandwidth. Experimental time histories of the pressure inside the reduced-section tube are plotted in Fig. 9.

4.4. The logarithmic potential

4.4.1. Design

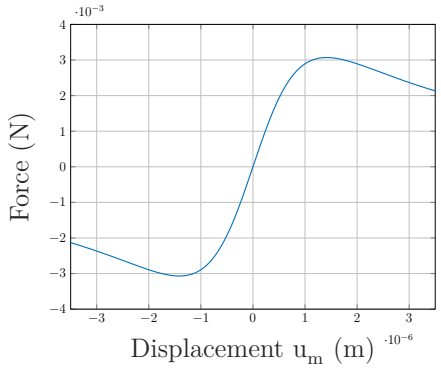

Figure 10: Logarithmic potential force $F_{\mathrm{NL}} = \frac{K_d u_m}{1+\beta_{\mathrm{NL}} u_m^2}$ with $\beta_{\mathrm{NL}} = 5 \times 10^{11}$ m^{-2}

To the best of our knowledge, the logarithmic potential force has not been experimentally implemented yet. It would create softening behavior that cannot become unstable [50]. Let us introduce the following potential

function:

$$V(u_m) = -\frac{1}{2} K_d \ln(1 + u_m^2) \tag{25}$$

A key point is that this force cannot cause unstable behaviors as the potential cannot become positive. It gives the equivalent nonlinear restoring force:

$$F_{\mathrm{NL}}(u_m) = \frac{K_d u_m}{1 + u_m^2} \tag{26}$$

Nevertheless, this nonlinear force in its current state activates a nonlinear behavior at high excitation amplitudes. In order to enable the activation of a nonlinear behavior at lower excitation amplitudes, we introduce a coefficient β_{NL} as follows:

$$F_{\mathrm{NL}}(u_m) = \frac{K_d u_m}{1 + \beta_{\mathrm{NL}} u_m^2} \tag{27}$$

The force is plotted Fig. 10 with $\beta_{\mathrm{NL}} = 5 \times 10^{11}$ m^{-2}. The logarithmic potential restoring force can be briefly studied by developing the Taylor series of the force:

$$F_{\mathrm{NL}}(u_m) = \frac{K_d u_m}{1 + \beta_{\mathrm{NL}} u_m^2} = \sum_{n=0}^{\infty} (-1)^n K_d \beta_{\mathrm{NL}}^n u_m^{2n+1} \tag{28}$$

The Taylor series of the force shows that logarithmic potential restoring force is equivalent to a cubic softening restoring force if the Taylor series is truncated to its two first terms. Therefore, the choice of a similar μ_K than chosen for the cubic behavior should give similar results. Let us choose $\mu_K = 1.5496$ which is the same as the cubic softening restoring force. Nevertheless, the Taylor series highlights that the logarithmic potential restoring force is weaker than the cubic softening restoring force [50]. Both behaviors are compared in Fig. 11a for equal parameters $|\beta_{\mathrm{NL}}| = 3 \times 10^{11}$ m^{-2} and $\mu_K = 1$. One can observe that the softening behavior is activated at higher amplitudes for equal parameters. Therefore, the logarithmic potential softening restoring force is weaker than the cubic softening behavior, as expected. To solve this issue, the value of β_{NL} should be raised, as depicted in Fig. 11b for $\mu_K = 1$, and $\beta_{\mathrm{NL}} = 5 \times 10^{11}$ for the logarithmic potential restoring force and $\beta_{\mathrm{NL}} = -3 \times 10^{11}$ m^{-2} for the cubic softening restoring force. The chosen parameters for the experiment are $\mu_M = 1$, $\mu_K = 1.5496$, $\mu_R = 1/8$ and $\beta_{\mathrm{NL}} = 5 \times 10^{-11}$ m^{-2}.

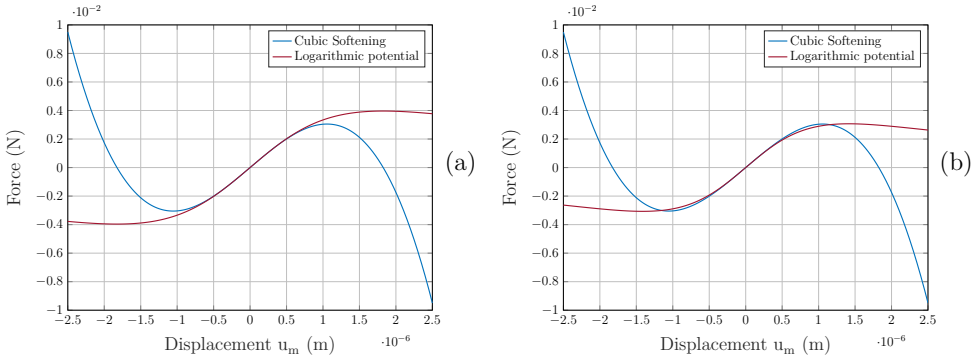

Figure 11: Restoring forces of the Logarithmic potential and Cubic Softening nonlinearities with (a) $|\beta_{\mathrm{NL}}| = 3 \times 10^{-11}$ m^{-2} (b) $\beta_{\mathrm{NL}} = 5 \times 10^{11}$ m^{-2} for the logarithmic potential restoring force and $\beta_{\mathrm{NL}} = -3 \times 10^{11}$ m^{-2} for the cubic softening resotoring force.

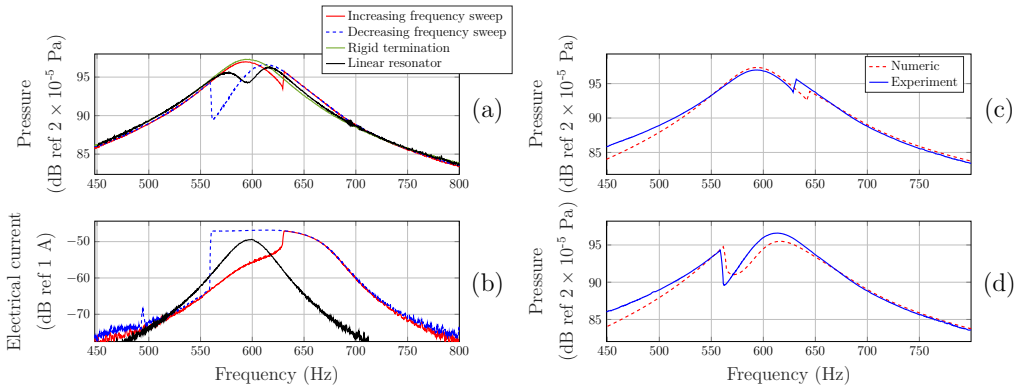

Figure 12: Experimental results for the logarithmic potential restoring force: variation of (a) the pressure amplitude, (b) the electrical current. Experimental and corresponding numerical results obtained from direct numerical integration of Eq. (19): variation of the pressure amplitude: (a) increasing frequency sweep (b) decreasing frequency sweep.

4.4.2. Results

The variations of the pressure and electrical current amplitudes are plotted in Figs. 12a and 12b for both increasing and decreasing frequency sweeps of the excitation. One can observe that the ER presents a softening behavior. Moreover, energy transfer from the acoustic mode of the tube to the nonlinear ER occurs at the frequencies of the nonlinear resonance, following the same phenomenon as the previous cases.

The numerical results obtained from the integration of Eq. (19) are com-

pared to experimental ones in Fig. 12c for the increasing frequency sweep, and in Fig. 12d for the decreasing frequency sweep. The numerical resolution of the model predicts well the behavior of the ER, despite the frequency shift of the jump, as for the other target behaviors. Despite the fractional nature of the restoring forcing function, it shows that the digital ER control is efficient in implementing the programmed nonlinear behaviors. The logarithmic potential restoring force shows great potential for sound absorption as the frequency bandwidth of efficiency is broadened. It also features sound absorption being equal to or greater than the linear oscillator.

As previously mentioned, the nonlinear behavior can be attained at higher

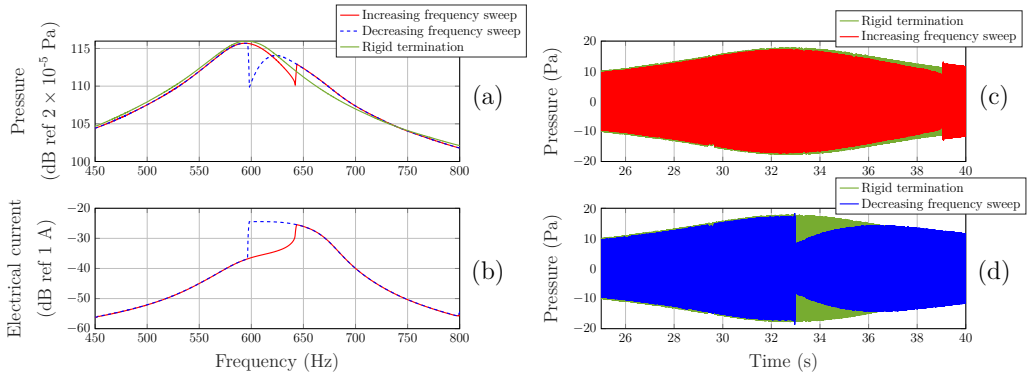

Figure 13: Experimental results for the logarithmic potential restoring force at high excitation amplitude with $\mu_M = 1$, $\mu_K = 1.5496$, $\mu_R = 1/8$ and $\beta_{\mathrm{NL}} = 3 \times 10^9$: variation of (a) the pressure amplitude, (b) the electrical current. Experimental time histories of the pressure inside the reduced-section tube with (c) increasing frequency sweep (d) decreasing frequency sweep.

or lower excitation amplitudes. It is due to the nonlinear parameter β_{NL} which determines the magnitude of the nonlinear term. The nonlinear term activates the nonlinear response when its order of magnitude becomes similar to the one of the linear term. Based on this analysis, let us choose the parameters $\mu_M = 1$, $\mu_K = 1.5496$, $\mu_R = 1/8$ and $\beta_{\mathrm{NL}} = 3 \times 10^9$. The variations of the pressure and electrical current amplitudes are plotted in Figs. 13a and 13b. One can observe that the nonlinear phenomena are reproduced at higher excitation amplitudes. It highlights a softening behavior. The time histories of the pressure inside the reduced-section tube are plotted for both increasing and decreasing frequency sweeps in Figs 13c and 13d.

5. Conclusion

The article features the programming of diverse nonlinear behaviors at low excitation amplitudes and their potential application for noise reduction purposes. A Real-Time-Based method and algorithm are employed to synthesize both polynomial and non-polynomial nonlinear behaviors. In this contribution, we test such control algorithm to achieve cubic, piece-wise linear, and logarithmic restoring forces, with comparison to numerical results. Piece-wise linear and logarithmic resonator dynamics are behaviors that are hardly achievable by passive means, even at high excitation levels, nevertheless, they are highly interesting applications. Observe that the logarithmic dynamics, while being fractional, can be implemented using this method. Moreover, the nonlinear ER is here for the first time tested against the attenuation of the primary acoustic mode of a coupled tube. This paper proves that our nonlinear ER correctly performs the expected trends for various target dynamics, in a coupled environment. Despite not being optimized, the nonlinear oscillators created in this study led to a significant noise reduction within the tube. To design the oscillators for efficient noise reduction purposes, an analytical study can be performed using the method of multiple scales [28, 52]. This perspective of study enables the programming of additional nonlinear phenomena. For example, the programming of compound piece-wise nonlinearities for multi-energy levels of activations, as discussed in [34], can be performed to create fast energy triggering. Moreover, non-periodic responses such as modulate [53] should be investigated. This paper is the first step toward the conception of a distributed set of nonlinear systems to create programmable nonlinear meta-materials for vibro-acoustical applications.

Acknowledgement

The authors would like to thank the following organizations for supporting this research: (i) The "Ministère de la transition écologique" and (ii) LABEX CELYA (ANR-10-LABX-0060) of the "Université de Lyon" within the program "Investissement d'Avenir" (ANR-11- IDEX-0007) operated by the French National Research Agency (ANR).

Appendix A. Model of the experiment

Appendix A.1. The influence of the non-modeled antiresonance

This appendix aims at explaining the differences between the model and the experiment. Taking into account the inevitable model uncertainties (in both ER and tube cavity models) of the simplified numerical model, the shift of the experimental bifurcation with respect to the numerical one is understandable. However, the low-frequency inaccuracy of the numerical results is due to an antiresonance of the tube cavity at lower frequencies than the acoustic mode of the tube, as depicted in Fig A.14. The model does not take into account the antiresonance at 115 Hz, which could impact the coupling with the ER, and consequently, it could contribute to the discrepancy between measurements and simulations. The influence of the antiresonance can not be ignored. Nevertheless, notice that slight pressure variations in the experimental set-up may trigger the bifurcation earlier or later than simulated with numerical means. Moreover, considering both the complexity of the actual system and the simplicity of the numerical model (reduced to one mode), the agreement between measurements and simulations is reasonable.

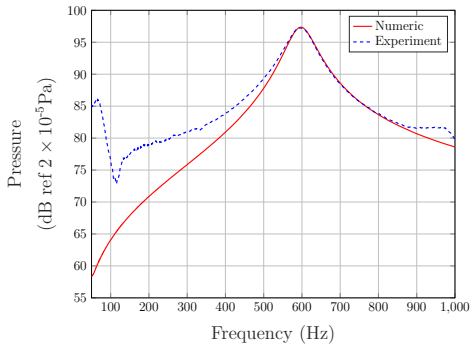

Figure A.14: Variation of the pressure amplitude inside the reduced-section tube with a rigid termination

Appendix A.2. The influence of the damping parameter

The form of the damping parameter of the primary system c_a has been chosen arbitrarily to model multiple physical damping phenomena. As a result, a preliminary study regarding its influence on the results is needed. The damping parameter is obtained using the rigid termination measurement.

The determination of its value has been done using three measurements at different excitation amplitudes. The value of the damping parameter is:

$$c_a = 0.0386 \pm 1.1 \times 10^{-4} \text{ kg.s}^{-1} \tag{A.1}$$

Let us consider the parameter $c_{a,p}$ such as $c_{a,p} \in [0.8c_a; 1.2c_a]$. Its definition takes into account a variation of 20% of c_a, which is larger than the calculated uncertainty. Let us plot the experimental data along with simulations realized with different values of $c_{a,p}$ in the case of a cubic hardening restoring force with $\mu_K = \mu_M = 1$, $\mu_R = 1/8$ and $\beta_{textNL} = 2 \times 10^{11}$ m^{-2}. The variation of the pressure amplitude inside the reduced-section tube is presented for increasing frequency sweep in Fig. A.15a, and decreasing frequency sweep in Fig. A.15b. One can observe that the bifurcation frequency changes depending on the damping parameter of the acoustic mode of the tube. The lower value of the parameter gives the lower frequency of bifurcation, and the higher value of the parameter gives the higher frequency of bifurcation. Moreover, let us plot the quality of the prediction of the

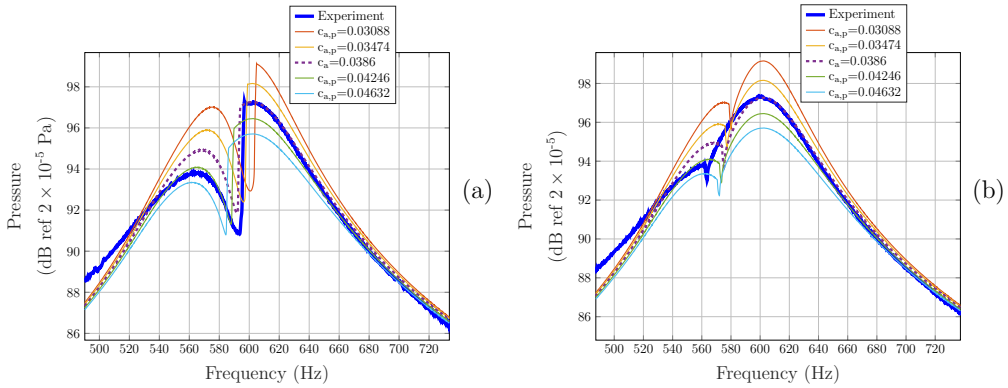

Figure A.15: Variation of the pressure amplitude inside the reduced-section tube as a function of frequency for multiple values of damping c_a with (a) increasing frequency sweep (b) decreasing frequency sweep.

simulations with each c_a using the classical indicator:

$$\text{Indicator} = \sum_i (x^i_{c_a} - y^i)^2 \tag{A.2}$$

where $x^i_{c_a}$ stands for the values of the pressure spectra predicted by simulations for each value of the damping parameter c_a. The variable y^i denotes

the values of the pressure spectra from experimental data. One can see in Fig. A.16 that the best value given by this indicator is the measured value $c_a = 0.0386$ kg.s^{-1}.

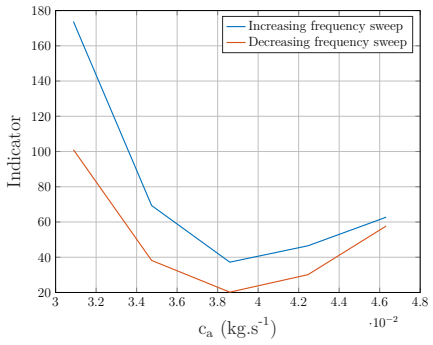

Figure A.16: Least mean square indicator of the difference of simulations done with multiple values of c_a

References

[1] P. Morse, Some Aspects of the Theory of Room Acoustics, J. Acoust. Soc. Am. 11 (1939) 56–66.

[2] M. E. Delany, E. N. Bazley, Acoustical properties of fibrous absorbent materials, Appl. Acoust. 3 (2) (1970) 105–116. doi:10.1016/0003-682X(70)90031-9.

[3] Y. Champoux, J. F. Allard, Dynamic tortuosity and bulk modulus in air-saturated porous media, J. Appl. Phys. 70 (4) (1991) 1975–1979. doi:10.1063/1.349482.

[4] C. Piégay, P. Glé, E. Gourdon, E. Gourlay, S. Marceau, Acoustical model of vegetal wools including two types of fibers, Appl. Acoust. 129 (2018) 36–46. doi:10.1016/j.apacoust.2017.06.021.

[5] D. Miljkovic, Active noise control: From analog to digital - Last 80 years, 2016 39th Int. Conv. Inf. Commun. Technol. Electron. Microelectron. MIPRO 2016 - Proc. (2016) 1151–1156doi:10.1109/MIPRO.2016.7522313.

[6] P. Lueg, Process of silencing sound oscillations, uS Patent 2043416 (3 1934).

[7] D. Guicking, Patents on Active Control of Sound and Vibration-an Overview, Tech. rep., Universitat Gottingen (2009).

[8] P. Gardonio, E. Bianchi, S. Elliott, Smart panel with multiple decentralized units for the control of sound transmission. Part I: theoretical predictions, J. Sound Vib. 274 (1-2) (2004) 163–192. doi:10.1016/j.jsv.2003.05.004.

[9] P. Gardonio, E. Bianchi, S. Elliott, Smart panel with multiple decentralized units for the control of sound transmission. Part II: design of the decentralized control units, J. Sound Vib. 274 (1-2) (2004) 193–213. doi:10.1016/j.jsv.2003.05.007.

[10] E. Bianchi, P. Gardonio, S. Elliott, Smart panel with multiple decentralized units for the control of sound transmission. Part III: control system implementation, J. Sound Vib. 274 (1-2) (2004) 215–232. doi:10.1016/j.jsv.2003.05.006.

[11] H. F. Olson, E. G. May, Electronic Sound Absorber, J. Acoust. Soc. Am. 25 (6) (1953) 1130–1136. doi:10.1121/1.1907249.

[12] D. Guicking, E. Lorenz, An active sound absorber with porous plate, J. Vib. Acoust. 106 (3) (1984) 389–392. doi:10.1115/1.3269206.

[13] D. Guicking, K. Karcher, Active impedance control for one-dimensional sound, J. Vib. Acoust. 106 (3) (1984) 393–396. doi:10.1115/1.3269207.

[14] M. Furstoss, D. Thenail, M. A. Galland, Surface impedance control for sound absorption: Direct and hybrid passive/ active strategies, J. Sound Vib. 203 (2) (1997) 219–236. doi:10.1006/JSVI.1996.0905.

[15] D. Thenail, O. Lacour, M. A. Galland, M. Furstoss, The Active Control of Wall Impedance, Acta Acust. 83 (1997) 1039–1044.

[16] M.-A. Galland, B. Mazeaud, N. Sellen, Hybrid passive/active absorbers for flow ducts, Appl. Acoust. 66 (6) (2005) 691–708. doi:10.1016/j.apacoust.2004.09.007.

[17] M. Collet, P. David, M. Berthillier, Active acoustical impedance using distributed electrodynamical transducers, J. Acoust. Soc. Am. 125 (2) (2009) 882–894. doi:10.1121/1.3026329.

[18] P. David, M. Collet, J. M. Cote, Experimental implementation of acoustic impedance control by a 2D network of distributed smart cells, Smart Mater. Struct. 19 (3) (2010). doi:10.1088/0964-1726/19/3/035028.

[19] S. Karkar, E. De Bono, M. Collet, G. Matten, M. Ouisse, E. Rivet, Broadband Nonreciprocal Acoustic Propagation Using Programmable Boundary Conditions: From Analytical Modeling to Experimental Implementation, Phys. Rev. Appl. 12 (5) (2019). doi:10.1103/PhysRevApplied.12.054033.

[20] E. Rivet, S. Karkar, H. Lissek, On the optimisation of multi-degree-of-freedom acoustic impedances of low-frequency electroacoustic absorbers for room modal equalisation, Acta Acust. united with Acust. 103 (6) (2017) 1025–1036. doi:10.3813/AAA.919132.

[21] R. Boulandet, H. Lissek, S. Karkar, M. Collet, G. Matten, M. Ouisse, M. Versaevel, Duct modes damping through an adjustable electroacoustic liner under grazing incidence, J. Sound Vib. 426 (2018) 19–33. doi:10.1016/j.jsv.2018.04.009.

[22] E. De Bono, M. Collet, G. Matten, S. Karkar, H. Lissek, M. Ouisse, K. Billon, T. Laurence, M. Volery, Effect of time delay on the impedance control of a pressure-based, current-driven Electroacoustic Absorber, J. Sound Vib. 537 (2022) 117201. doi:10.1016/J.JSV.2022.117201.

[23] K. Billon, E. D. Bono, M. Perez, E. Salze, G. Matten, M. Gillet, M. Ouisse, M. Volery, H. Lissek, J. Mardjono, M. Collet, In flow acoustic characterisation of a 2D active liner with local and non local strategies., Appl. Acoust. 191 (2022) 108655. doi:10.1016/j.apacoust.2022.108655.

[24] S. Sergeev, R. Fleury, H. Lissek, Ultrabroadband sound control with deep-subwavelength plasmacoustic metalayers, Nat. Commun. 14 (1) (2023) 2874. doi:10.1038/s41467-023-38522-5.

[25] G. Gatti, M. Brennan, B. Tang, Some diverse examples of exploiting the beneficial effects of geometric stiffness nonlinearity, Mech. Syst. Signal Process. 125 (2019) 4–20. doi:10.1016/j.ymssp.2018.08.024.

[26] A. F. Vakakis, O. V. Gendelman, L. A. Bergman, D. M. McFarland, G. Kerschen, Y. S. Lee, Nonlinear Targeted Energy Transfer in Mechanical and Structural Systems I & II, Springer, 2009.

[27] I. Kovacic, M. J. M. J. Brennan, The Duffing equation : nonlinear oscillators and their phenomena, John Wiley & Sons, Ltd, 2011. doi:10.1002/9780470977859.

[28] A. H. Nayfeh, D. T. Mook, Nonlinear Oscillations, John Wiley & Sons, Ltd, 1995.

[29] F. Georgiadis, A. F. Vakakis, D. M. Mcfarland, L. Bergman, Shock isolation through passive energy pumping caused by nonsmooth nonlinearities, Int. J. Bifurc. Chaos 15 (06) (2005) 1989–2001. doi:10.1142/S0218127405013101.

[30] O. V. Gendelman, Y. Starosvetsky, M. Feldman, Attractors of harmonically forced linear oscillator with attached nonlinear energy sink I: Description of response regimes, Nonlinear Dyn. 51 (1-2) (2008) 31–46. doi:10.1007/s11071-006-9167-0.

[31] C.-H. Lamarque, O. V. Gendelman, A. Ture Savadkoohi, E. Etcheverria, Targeted energy transfer in mechanical systems by means of non-smooth nonlinear energy sink, Acta Mech. 221 (1-2) (2011) 175–200. doi:10.1007/s00707-011-0492-0.

[32] G. Hurel, A. Ture Savadkoohi, C. H. Lamarque, Passive control of a two degrees-of-freedom pendulum by a non-smooth absorber, Nonlinear Dyn. 98 (4) (2019) 3025–3036. doi:10.1007/S11071-019-04891-0.

[33] G. Hurel, A. Ture Savadkoohi, C. H. Lamarque, Design of a nonlinear absorber for a 2 degrees of freedom pendulum and experimental validation, Struct. Control Heal. Monit. 28 (11) (2021). doi:10.1002/STC.2814.

[34] C. da Silveira Zanin, A. Ture Savadkoohi, S. Baguet, R. Dufour, G. Hurel, Nonlinear vibratory energy exchanges in a meta-cell, Int. J. Non. Linear. Mech. 146 (2022) 104148. doi:10.1016/j.ijnonlinmec.2022.104148.

[35] O. Gendelman, Analytic treatment of a system with a vibro-impact nonlinear energy sink, J. Sound Vib. 331 (21) (2012) 4599–4608. doi:10.1016/j.jsv.2012.05.021.

[36] E. Gourc, G. Michon, S. Seguy, A. Berlioz, Targeted Energy Transfer Under Harmonic Forcing With a Vibro-Impact Nonlinear Energy Sink: Analytical and Experimental Developments, J. Vib. Acoust. 137 (3) (2015). doi:10.1115/1.4029285.

[37] B. Cochelin, P. Herzog, P. O. Mattei, Experimental evidence of energy pumping in acoustics, C. R. Méc. 334 (11) (2006) 639–644. doi:10.1016/j.crme.2006.08.005.

[38] R. Bellet, B. Cochelin, P. Herzog, P. O. Mattei, Experimental study of targeted energy transfer from an acoustic system to a nonlinear membrane absorber, J. Sound Vib. 329 (14) (2010) 2768–2791. doi:10.1016/j.jsv.2010.01.029.

[39] E. Gourdon, A. Ture Savadkoohi, V. Alamo Vargas, Targeted energy transfer from one acoustical mode to an helmholtz resonator with nonlinear behavior, J. Vib. Acoust. 140 (6) (2018). doi:10.1115/1.4039960.

[40] V. Alamo Vargas, E. Gourdon, A. Ture Savadkoohi, Nonlinear softening and hardening behavior in Helmholtz resonators for nonlinear regimes, Nonlinear Dyn. 91 (1) (2018) 217–231. doi:10.1007/s11071-017-3864-8.

[41] D. Bitar, E. Gourdon, C. H. Lamarque, M. Collet, Shunt loudspeaker using nonlinear energy sink, J. Sound Vib. 456 (2019) 254–271. doi:10.1016/j.jsv.2019.05.021.

[42] X. Guo, H. Lissek, R. Fleury, Improving Sound Absorption Through Nonlinear Active Electroacoustic Resonators, Phys. Rev. Appl. 13 (1) (2020). doi:10.1103/PhysRevApplied.13.014018.

[43] E. De Bono, M. Morell, M. Collet, E. Gourdon, A. T. Savadkoohi, M. Ouisse, C. Lamarque, Model-inversion control to enforce tunable duffing-like acoustical response on an electroacoustic resonator at low excitation levels, J. Sound Vib. (2023) 118070doi:10.1016/j.jsv.2023.118070.

[44] G. C. Goodwin, S. F. Graebe, M. E. Salgado, Control System Design, Vol. 27, Prentice Hall, New Jersey, 2000.

[45] C. E. da Silveira Zanin, A. Labetoulle, E. De Bono, E. Gourdon, M. Collet, A. Ture Savadkoohi, Experimental evidences of nonlinear programmable electroacoustic loudspeaker, Build. Acoust. 30 (3) (2023) 249–263. doi:10.1177/1351010X231184040.

[46] L. L. Beranek, T. J. Mellow, Acoustics: Sound Fields and Transducers, Academic Press, 2012.

[47] R. D. Blevins, Formulas for natural frequency and mode shape, Van Nostrand Reinhold Ltd, 1979.

[48] D. J. Ewins, Modal Testing: Theory, Practice and Application, John Wiley & Sons, Ltd, 2000.

[49] M. Weiss, B. Vaurigaud, A. Ture Savadkoohi, C.-H. Lamarque, Control of vertical oscillations of a cable by a piecewise linear absorber, J. Sound Vib. 435 (2018) 281–300. doi:10.1016/j.jsv.2018.07.033.

[50] O. V. Gendelman, Targeted energy transfer in systems with non-polynomial nonlinearity, J. Sound Vib. 315 (3) (2008) 732–745. doi:10.1016/j.jsv.2007.12.024.

[51] A. Labetoulle, A. Ture Savadkoohi, E. Gourdon, Detection of different dynamics of two coupled oscillators including a time-dependent cubic nonlinearity, Acta Mech. 233 (1) (2022) 259–290. doi:10.1007/s00707-021-03119-w.

[52] A. Ture Savadkoohi, C.-H. Lamarque, M. Contessa, Trapping vibratory energy of main linear structures by coupling light systems with geometrical and material non-linearities, Int. J. Non. Linear. Mech. 80 (2016) 3–13. doi:10.1016/j.ijnonlinmec.2015.11.011.

[53] Y. Starosvetsky, O. Gendelman, Strongly modulated response in forced 2DOF oscillatory system with essential mass and potential asymmetry, Phys. D Nonlinear Phenom. 237 (13) (2008) 1719–1733. doi:10.1016/j.physd.2008.01.019.